



## PAPER

## Performance evaluation of HiPET, a high sensitivity and high resolution preclinical PET tomograph

RECEIVED  
13 September 2019REVISED  
24 December 2019ACCEPTED FOR PUBLICATION  
14 January 2020PUBLISHED  
12 February 2020Zheng Gu<sup>1,2,4</sup>, Richard Taschereau<sup>1</sup>, Nam T Vu<sup>2</sup>, David L Prout<sup>1</sup>, Jason Lee<sup>1,3</sup> and Arion F Chatzioannou<sup>1,2,3</sup><sup>1</sup> Crump Institute for Molecular Imaging, David Geffen School of Medicine, University of California, Los Angeles, Los Angeles, CA, United States of America<sup>2</sup> Sofie Biosciences, Culver City, California, United States of America<sup>3</sup> Jonsson Comprehensive Cancer Center, University of California, Los Angeles, Los Angeles, CA, United States of America<sup>4</sup> Author to whom any correspondence should be addressed.E-mail: [zhgu@mednet.ucla.edu](mailto:zhgu@mednet.ucla.edu)**Keywords:** small animal imaging, PET, performance evaluation, instrumentation, molecular imaging**Abstract**

HiPET is a recently developed prototype preclinical PET scanner dedicated to high sensitivity and high resolution molecular imaging. The HiPET system employs a phoswich depth of interaction (DOI) detector design, which also allows identification of the large majority of the cross layer crystal scatter (CLCS) events. This work evaluates its performance characteristics following the National Electrical Manufacturers Association (NEMA) NU4-2008 protocol.

The HiPET consists of twenty flat panel type detectors arranged in two rings. The inner diameter is 160 mm and the axial field of view (FOV) is 104 mm. Each detector is comprised of two layers of phoswich scintillator crystal arrays, a tapered, pixelated glass lightguide and a multi anode photomultiplier tube (MAPMT). The front (gamma ray entrance) layer is a  $48 \times 48$  pixelated cerium doped lutetium yttrium orthosilicate (LYSO) scintillator array with individual crystals measuring  $1.01 \times 1.01 \times 6.1$  mm. The back (towards the PMT) layer is a  $32 \times 32$  pixelated bismuth germanate (BGO) scintillator array with individual crystals measuring  $1.55 \times 1.55 \times 8.9$  mm.

For energy windows of 250–650 keV and 350–650 keV, the peak absolute sensitivity at the center of the FOV was 13.5% and 10.4% including CLCS events, and 11.8% and 8.9% excluding CLCS events, respectively. The average detector energy resolution derived by averaging the individual crystal spectra was  $11.7\% \pm 1.4\%$  for LYSO and  $17.0\% \pm 1.4\%$  for BGO. The 3D ordered-subsets expectation maximization (OSEM) reconstructed image of a point source in air, ranged from 0.73 mm to 1.19 mm, with an average value of  $0.93 \pm 0.09$  mm at all measured locations. The peak noise equivalent count rate (NECR) and scatter fraction were 179 kcps at 12.4 MBq and 6.9% for the mouse-sized phantom, and 63 kcps at 11.3 MBq and 18.3% for the rat-sized phantom. For the NEMA image quality phantom, the uniformity was 5.8%, and the spillover ratios measured in the water- and air-filled cold region chambers were 0.047 and 0.044, respectively. The recovery coefficients (RC) ranged from 0.31 to 0.92.

These results and *in vivo* evaluation demonstrate that the HiPET can achieve high quality molecular imaging for biomedical applications.

**Introduction**

Small animal positron emission tomography (PET) has been a driving force in molecular imaging, enabling the characterization and understanding of biological processes at the cellular and molecular level (Phelps 2000, Weissleder and Mahmood 2001, Chatzioannou 2002). The use of small animals such as mice and rats as experimental models for a large variety of applications in pharmacology, cancer biology, immunology, pathology, neuroscience and cardiology demands preclinical PET scanners that have ever higher resolution and sensitivity, to visualize subtle PET tracer biodistribution and expand the repertoire of available imaging agents (Cherry 2004). Advances in spatial resolution and sensitivity of imaging systems can enable applications such as imaging

subcortical structures of the mouse brain, detecting early lesions, metastasis and tissue heterogeneity in clinically relevant models of cancer, and providing access to new biological targets and pathways (Cherry 2006). Therefore, high sensitivity and high resolution have been pursued as some of the most important and longstanding research goals for preclinical PET imaging (Lewellen 2008).

For PET systems that employ conventional pixelated scintillator detectors, the spatial resolution is determined by the cross section of the scintillator crystal elements, and the sensitivity can be increased by using long crystals for higher 511 keV gamma photon detection efficiency. Unfortunately, long and narrow crystals in a small diameter gantry lead to increased penetration of oblique incident gamma rays before interaction. This causes event mispositioning also called parallax error, degrading the spatial resolution uniformity and distorting the appearance of the source (Hoffman *et al* 1989). Inter-crystal scatter (ICS) events, for which the incoming annihilation photons interact with more than one detection element within the same block detector, is another cause of event mispositioning in addition to the parallax error. With conventional PET detector designs that employ Anger logic positioning schemes (Anger 1958), the spatial coordinates of such ICS events corresponding to the energy weighted mean of the multiple interaction sites are different from the location of first interaction. As a result, this positioning error of the corresponding line of response leads to degradation of the lesion detectability and quantitative characteristics of an imaging system (Levin *et al* 1997, Gu *et al* 2010).

Much effort has been devoted over the past several years to pursue high resolution and high sensitivity of PET by developing detectors with the capability of encoding the depth of annihilation photon interaction (DOI) (Wong 1986, Moses and Derenzo 1994, Murayama *et al* 1998, Yamamoto and Ishibashi 1998, Seidel *et al* 1999, Saoudi *et al* 1999, Zhang *et al* 2003, Tsuda *et al* 2004, McElroy *et al* 2005, Yang *et al* 2006, Inadama *et al* 2006, Mosset *et al* 2006, Ling *et al* 2007, Du *et al* 2009, Vandenbroucke *et al* 2010, Gu *et al* 2011, Yazaki *et al* 2012, Shao *et al* 2014) and investigating the methodologies of rejecting ICS events, or estimating the first interaction site of an ICS event for improved image quality and quantification (Comanor *et al* 1996, Shao *et al* 1996, Miyaoka and Lewellen 2000, Pratz and Levin 2009, Gu *et al* 2010, Ritzer *et al* 2017). Recently, we developed HiPET, a new high resolution and high sensitivity preclinical PET tomograph, at the UCLA Crump Institute for Molecular Imaging. The HiPET prototype system employs a dual layer LYSO/BGO (cerium doped lutetium yttrium orthosilicate/bismuth germanate) phoswich DOI detector design (Gu *et al* 2015a, Hadjioannou *et al* 2019) to retrieve DOI information that improves spatial resolution uniformity across the field of view (FOV). Furthermore, this detector allows identification of the majority of the cross layer crystal scatter (CLCS) events (the ICS events that deposit their energy in both layers), allowing a great reduction of this source of error.

This work characterizes the overall performance of the HiPET system following the National Electrical Manufacturers Association (NEMA) NU 4-2008 standards (National Electrical Manufacturers Association 2008) where possible. Studies of sensitivity, spatial resolution, energy resolution, timing resolution, scatter fraction (SF) and count-rate performance were performed for HiPET and compared to other small animal PET scanners. A variety of dedicated phantom and *in vivo* rodent studies were acquired to demonstrate the capability of the HiPET for high sensitivity, high resolution translational molecular imaging applications.

## Materials and methods

### System description

A photograph of the prototype HiPET scanner is shown in figure 1(A). The HiPET system consists of twenty flat panel detectors arranged in two rings. The detector ring inner diameter is 160 mm and the axial FOV is 104 mm. Each detector is comprised of two layers of pixelated scintillator arrays (Proteus, Chagrin Falls, OH), a multi-element glass lightguide and a multianode photomultiplier tube (MAPMT), as shown in figure 1(B). The front (annihilation photon entrance) scintillator layer is a  $48 \times 48$  array of  $1.01 \times 1.01 \times 6.1$  mm LYSO crystals (1.09 mm pitch). The back layer is a  $32 \times 32$  array of  $1.55 \times 1.55 \times 8.9$  mm BGO crystals (1.63 mm pitch). LYSO and BGO scintillator elements are multiplexed in a ratio of 9:4, with each  $3 \times 3$  LYSO array segment being coupled to a  $2 \times 2$  BGO array segment. The LYSO and BGO crystal elements were mechanically polished on all sides except of the ends towards the lightguide, which were diffusely ground. Each individual crystal was bonded with a specular optical reflector (3M, St Paul, MN). A tapered, multiple-element glass lightguide (Gu *et al* 2015a) was used to couple the exit end of the BGO crystal array ( $52 \times 52$  mm) to the photosensitive area ( $46 \times 46$  mm) of a H12700 flat panel type MAPMT (Hamamatsu Photonics, Bridgewater, NJ). The complete detector module has overall dimensions of  $52 \times 52$  mm matching the external dimensions of the PMT package, allowing continuous positioning of the scintillator arrays and the creation of flat panel detectors without gaps between detector modules. The scintillator array, lightguide and MAPMT were permanently bonded with epoxy.

A charge-division resistor network (Siegel *et al* 1996) was used to convert the 64 anode outputs from each MAPMT to one energy and two position signals (*X* and *Y*). Due to the large difference of scintillation light output and decay time between LYSO and BGO (35 000 photons/MeV versus 8000 photons/MeV; 42 ns versus 300 ns decay constant), the peak amplitude of the raw LYSO signal waveform is 20–30 times larger than that of the BGO

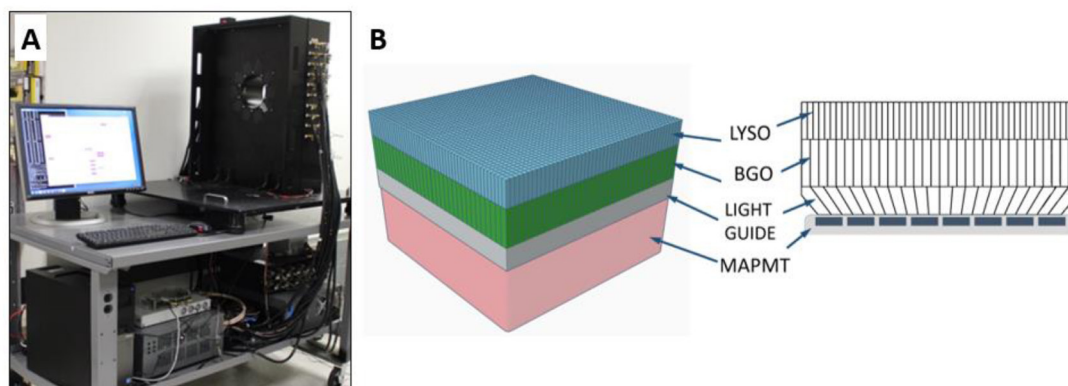
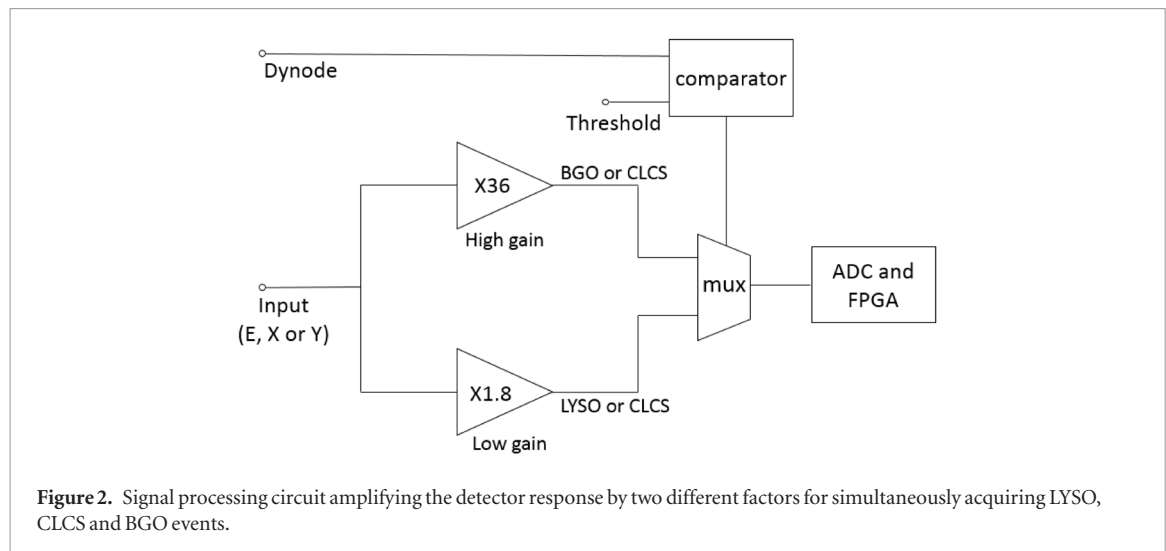


**Figure 1.** (A) Photograph of the HiPET system; (B) schematic and cross-section of the DOI detector.

signal. To fit the LYSO signal within the dynamic range of the free running analog-to-digital converters (ADC) (PicoDigitizer, Nutaq, Quebec), overall signal amplification is kept low. For the BGO signal, this amplification is not enough to overcome electronic noise, degrading the position decoding accuracy of the BGO events. To retrieve accurate information simultaneously from both the LYSO and BGO signals, the DOI detector utilizes a readout circuit which amplifies the detector response by two different factors, along two different paths as shown in figure 2. The BGO events are detected from the path amplified with higher gain ( $\times 36$ ), while the LYSO events are detected from the path with lower gain ( $\times 1.8$ ). The CLCS events may be detected from either the high gain or low gain path, depending on the amount of energy deposited in the LYSO layer. The dynode signal from the DOI detector is compared with a preset threshold for selecting high gain or low gain path through a multiplexer, allowing operation with only three analog to digital channels per detector.

The Energy, X and Y signals from all twenty detectors were digitized by sixty 120 MHz free running ADCs at 14 bits per sample (PicoDigitizer, Nutaq, Quebec). These digital samples were processed in a Xilinx Virtex-6 field programmable gate array (FPGA, Xilinx, San Jose, CA) in real time for triggering, timing, energy and position calculation, and pulse shape discrimination. To determine the type of event (LYSO, BGO or CLCS) detected by the HiPET detectors, we applied the delayed charge integration (DCI) technique, a decision algorithm that relies on the measured composite light decay by two scintillators (LYSO = 42 ns, BGO = 300 ns) (Gu et al 2015a). Each event trigger starts a blocking time, within which the pulse is processed for DCI and no more events are allowed to trigger. The length of the trigger blocking time is related to detector dead time. Since in the HiPET detectors, most of the low gain events are LYSO events with short pulse duration ( $\sim 200$  ns), the trigger blocking time for the low gain path was set to 240 ns to decrease the detector dead time, while the blocking time for the high gain path was set to 1000 ns for detecting BGO events. During event processing, the measured energy waveform is partially integrated with two time intervals for acquiring DCI: an early integral of 0–192 ns and a later integral of 192–232 ns for the low gain path, and an early integral of 0–192 ns and a later integral of 192–800 ns for the high gain path. The ratio of the later integral to the early integral reflects the pulse shape and is used for event type identification as LYSO, BGO or CLCS, which is then encoded in the list mode file. A 160 ns large global timing window was applied in the FPGA logic and events in this window were recorded in the list mode file for post processing.

Coincidence and random event sorting were performed offline in software. In this work, the coincidence timing window was set to 20, 15 and 8 ns for BGO-BGO, LYSO-BGO and LYSO-LYSO event pairs. The event pairs outside of the corresponding coincidence timing windows but in the 160 ns large timing window were labeled as random events, therefore the delayed timing window for estimating and correcting for random coincidences was 140, 145 and 152 ns for BGO-BGO, LYSO-BGO and LYSO-LYSO event pairs. The size of the coincidence timing window was set close to 6 times of the standard deviation of the coincidence timing spectra (the range covering 99.7% of the Gaussian distribution). No obvious tail from the coincidence timing spectra was observed in the random timing window. Energy discrimination was not applied in the FPGA, allowing the energy window to be applied or varied offline in software postprocessing. Unless stated otherwise, all measurements for the single layer events (BGO or LYSO) in this work were processed with an energy window of 350–650 keV for both the LYSO (calibrated for the low gain path) and BGO (calibrated for the high gain path) events. The only exception to this was the sensitivity measurement, for which the LLD of the energy window for the LYSO and BGO events varied between 150 and 350 keV to show the influence of energy window on sensitivity. For the CLCS events, an upper level discriminator (ULD) corresponding to 550 keV of an LYSO event was applied to CLCS events detected from the low gain path, and a lower level discriminator (LLD) corresponding to 400 keV of a BGO event was applied to CLCS events detected from the high gain path. These thresholds were chosen in order to include the CLCS events that deposit 511 keV energy in the detector, as measured by either the low or the high gain path.



Component-based normalization (Mumcuoglu *et al* 1994) was applied to compensate for the differences in individual detector efficiencies, estimated from measurements of a cylindrical source filled with  $^{18}\text{F}$ . Fully 3D tomographic images were reconstructed by a 3D ordered-subset expectation maximization (OSEM) algorithm with incorporation of a system model based on a parameterized detector response. A total of 24 full iterations and 10 subsets were used for image reconstruction with regularization (Huber, hyperparameter value 0.05) and no post-reconstruction smoothing was applied. The characteristics of the HiPET systems are summarized in table 1.

### Energy and timing resolution

A cylindrical phantom with a diameter of 37 mm and 117 mm length was filled with 3.7 MBq (100  $\mu\text{Ci}$ )  $^{18}\text{F}$  and placed at the center of the field of view (CFOV). Energy spectra of individual crystals were extracted, and a Gaussian function was fitted to the photopeak of each energy spectra. Energy resolution was measured for every crystal in the scanner as the full width at half-maximum (FWHM) of the Gaussian function divided by the energy corresponding to the center of the photopeak, expressed as a percentage resolution. Timing spectra between different detector pairs and event types were extracted and a Gaussian function was fitted to the peak of each timing spectra. Timing resolution was measured as the FWHM of the Gaussian function.

### Spatial resolution

A 0.16 MBq  $^{22}\text{Na}$  point source with a nominal size of 0.3 mm, embedded in a 1 cm<sup>3</sup> piece of acrylic was used (NEMA NU4 compliant, Eckert & Ziegler Isotope Products, Valencia, CA). The point source was imaged at two axial locations: (a) the center of the axial FOV and (b) one fourth of the axial FOV, at 26 mm from the center along the axial direction. For each of these two axial locations, the source was placed radially offset at 0 mm, 5 mm, 10 mm, 15 mm, 25 mm and 50 mm from the geometric axis. Acquisition time was 60 min at each position and more than  $10^5$  prompt counts were acquired per measurement. Following the NEMA protocol, images were reconstructed using the filtered backprojection with reprojection (FBP 3DRP) method (Kinahan and Rogers 1989). In addition, images were reconstructed using the 3D OSEM algorithm. The point source response function was formed by summing 1D profiles parallel to the radial, tangential, and axial directions of the reconstructed image. A parabolic fit of the peak point and its two nearest neighboring points was used to determine the maximum value of the response function. Linear interpolation between adjacent pixels was used to determine the position of the half and one tenth of the parabolic curve maximum. Measurements were not corrected for the physical source dimensions, positron range, or non-collinearity of positron annihilation gammas.

### Sensitivity

The  $^{22}\text{Na}$  point source used in the spatial resolution measurement was also used to measure absolute system sensitivity. The activity of the point source was 0.16 MBq, low enough so that the counting loss due to deadtime was less than one percent and the random event rate was less than 5% of the true event rate, fulfilling the NEMA NU 4 recommendations. The axial sensitivity profile was measured with the  $^{22}\text{Na}$  source stepped from end to end of the axial FOV. The number of coincidences was recorded at each position for 60 min. Random events were subtracted from prompts before the true coincidences were divided by the actual source activity. This ratio was corrected for the branching ratio of  $^{22}\text{Na}$  (0.906), but the attenuation of the acrylic material surrounding the source was not compensated. The average sensitivity for a mouse-sized object (with a 7 cm axial length) and a rat-sized object (with the system axial length, 10.4 cm) was calculated from the measured axial sensitivity profile.

**Table 1.** Characteristics of the HiPET system, units of mm.

Crystal material	LYSO/BGO
Crystal size (mm)	$1.01 \times 1.01 \times 6.1/1.55 \times 1.55 \times 8.9$
Crystal pitch (mm)	1.09/1.63
Crystal array	$48 \times 48/32 \times 32$ crystals/PMT
Light guide	Tapered, pixelated light guide
PMT	Hamamatsu H12700 MAPMT
Number of detector modules	20
Number of crystals per module	3328
Number of crystals in total	66 560
Ring diameter (mm)	160
Axial FOV (mm)	104
Transaxial FOV (mm)	131
Number of ADCs	60
Signal processing system	PicoDigitizer (Nutaq, Quebec)
Number of LORs	$1.1 \times 10^9$

### Scatter and count-rate performance

The count-rate performance was evaluated using the NEMA NU-4 mouse- and rat-sized phantoms. The mouse-sized phantom is a 70 mm long and 25 mm diameter solid cylinder, with a cylindrical 3.2 mm diameter hole drilled parallel to the central axis at a radial offset of 10 mm. The rat-sized phantom is a 150 mm long and 50 mm diameter solid cylinder, with a cylindrical 3.2 mm diameter hole drilled parallel to the central axis at a radial offset of 17.5 mm. These solid cylinders are made of high density polyethylene ( $0.96 \text{ g cm}^{-3}$ ). A flexible tubing filled with  $^{18}\text{F}$  solution was inserted into the 3.2 mm cylindrical hole of the phantom. The initial activity was measured to be 14.1 and 17.6 MBq for the mouse- and rat-sized phantom respectively using a dose calibrator (Atomlab 300; Biodex Medical Systems, Upton, NY) at the start of the acquisition. Because the crystals in HiPET contain  $^{176}\text{Lu}$  that has intrinsic activity, background was measured in separate 60 min acquisitions for both phantoms.

The data was post-processed with an energy window of 350–650 keV and timing windows of 8/15/20 ns for the LYSO-LYSO/LYSO-BGO/BGO-BGO coincidences, and with the CLCS events excluded. As specified by NEMA NU-4, the scatter count rate was calculated by equation (1):

$$R_{\text{scatter}} = R_{\text{prompt}} - R_{\text{true}} - R_{\text{random}} - R_{\text{intrinsic}}, \quad (1)$$

where  $R_{\text{scatter}}$ ,  $R_{\text{prompt}}$ ,  $R_{\text{true}}$  and  $R_{\text{random}}$  are the scatter, prompt, true and random count rates respectively, and  $R_{\text{intrinsic}}$  is the intrinsic count rate of the scanner obtained from the background measurement. The SF was calculated by equation (2):

$$\text{SF} = \frac{R_{\text{scatter}}}{R_{\text{scatter}} + R_{\text{true}}}. \quad (2)$$

The NECR was defined by equation (3):

$$\text{NECR} = \frac{R_{\text{true}}^2}{R_{\text{prompt}} + k \times R_{\text{random}}} \quad (3)$$

where  $k$  relates to the statistical noise level in the estimate of the number of random events and equals to the ratio of the size of the coincidence timing window to the size of the delayed random window. Because the size of the delayed window used to estimate random events is about one order of magnitude larger than the size of the coincidence timing window, the statistical noise in the estimate of the number of random events is small in comparison to that in the traditional method where identical size of coincidence and delayed timing windows are used for direct random event subtraction. Following the NEMA NU-4 protocol, the noise equivalent count rate (NECR) was approximately determined by equation (4):

$$\text{NECR} \approx \frac{R_{\text{true}}^2}{R_{\text{prompt}}} = \frac{(R_{\text{prompt}} - R_{\text{random}} - R_{\text{intrinsic}})^2 \times (1 - \text{SF})^2}{R_{\text{prompt}}}. \quad (4)$$

### Imaging studies

For all imaging studies in this work, the data was post-processed with an energy window of 350–650 keV and a timing window of 8/15/20 ns for the LYSO-LYSO/LYSO-BGO/BGO-BGO coincidences, and with the CLCS events excluded.

### *NEMA image quality phantom study*

Image quality studies were performed using the NEMA NU-4 image quality phantom (Data Spectrum Corporation, Hillsborough, NC). The phantom was filled with 3.7 MBq of  $^{18}\text{F}$  solution and data was acquired for 20 min as prescribed in the NEMA NU-4 protocol. Detector efficiency normalization and random event corrections were applied, but no scatter correction was applied. A CT scan of the phantom and its supporting bed was acquired and the reconstructed CT image defining the data acquisition geometry was forward projected through the PET system response matrix to generate attenuation correction for the PET data.

A 22.5 mm-diameter and 10 mm-high cylindrical volume of interest (VOI) was drawn over the center of the uniform region of the image-quality phantom. The average concentration values and standard deviation (SD) in this VOI were used to estimate the uniformity performance as a measure of noise. The image slices covering the central 10 mm length of the rods were averaged to obtain a single 2D image slice of lower noise. Circular regions of interest (ROIs) were drawn in this 2D image around each rod, with diameters twice the physical diameters of the rods. The maximum values in each of these ROIs were measured and divided by the mean value obtained in the uniformity test to obtain the recovery coefficient (RC) for each rod size. The transverse image pixel coordinates of the locations with the maximum ROI values were recorded and used to create 10 mm long line profiles along the rods in the axial direction. The SD of the pixel values measured along each of these line profiles was calculated. Although no object scatter correction was applied to the acquired dataset, the spillover ratio of the water- and air-filled cold region chamber were calculated as specified in the NEMA NU-4 standard to provide a rough estimation of the photon scatter effects. The diameter of the VOI was 4 mm and encompassed the central 7.5 mm in length in the axial direction. The ratio of the mean in each cold region to the mean of the hot uniform area was reported as spillover ratio.

### *Hot rod phantom*

Spatial resolution was also assessed with a Derenzo style hot rod phantom with fillable channels of different diameters (0.8, 1.0, 1.25, 1.5, 2.0, and 2.5 mm) and center-to-center spacing two times the diameter of the respective channels (Cox *et al* 2016). The phantom was filled with 0.93 MBq of  $^{18}\text{F}$  at the start of the acquisition and scanned for 109 min. The data was reconstructed using 3D OSEM iterative reconstruction with a voxel size of  $0.27 \times 0.27 \times 0.27 \text{ mm}^3$ . Normalization and attenuation correction were applied. OSEM iterations were set to 24 using 10 subsets with Huber regularization (hyperparameter value 0.05).

### *Mouse study*

Animal studies were approved by the UCLA Animal Research Committee and carried out according to the guidelines of the Department of Laboratory Animal Medicine at UCLA. Animals were kept warm on heating pads throughout the imaging procedures. C57BL6 mice were consciously injected intravenously via tail vein with approximately 11.1 MBq (300  $\mu\text{Ci}$ ) [ $^{18}\text{F}$ ] FDG followed 15 min later by 45 min unconscious biodistribution under 2% isoflurane in oxygen. Mice were then transferred to a dedicated imaging chamber for PET/CT imaging under anesthesia. PET scans were acquired for 20 min with an energy window of 350–650 keV reconstructed using 3D OSEM, followed by CT acquisition on the CrumpCAT microCT (Taschereau *et al* 2014). All PET images were corrected for CT-based photon attenuation, detector normalization and radioisotope decay (scatter correction was not applied) and converted to units of percent injected dose per gram (%ID/g). Images were analyzed using AMIDE v1.0.4 (Loening and Gambhir 2003).

## Results

### **Energy and timing resolution**

For the crystals in all twenty detectors, the average energy resolution as derived by averaging the energy resolution of the individual crystal spectra, was  $11.7\% \pm 1.4\%$  for LYSO and  $17.0\% \pm 1.4\%$  for BGO. Crystal energy spectra representing the average energy resolution are shown in figure 3(A) (LYSO) and (B) (BGO). The coincidence timing resolution was  $2.2 \pm 0.2 \text{ ns}$ ,  $4.8 \pm 0.3 \text{ ns}$  and  $6.6 \pm 0.8 \text{ ns}$  for LYSO-LYSO, LYSO-BGO and BGO-BGO coincidences, respectively. Representative timing spectra for different event types are shown in figure 3(C).

### **Spatial resolution**

Figure 4 shows the 3D OSEM reconstructed image spatial resolution in the radial, tangential, and axial directions measured in the transverse plane at the axial center and at 1/4 axial offset. The spatial resolution has a range of 0.73 mm to 1.19 mm, with an average value of  $0.93 \pm 0.09 \text{ mm}$ . The Full width tenth maximum (FWTM) has a range of 1.56 mm to 2.37 mm, with an average value of  $1.94 \pm 0.17 \text{ mm}$ . The volumetric resolution varies from 0.66 to 0.96  $\mu\text{l}$ . The DOI measurement helps maintain a uniform spatial resolution over the entire imaging FOV. Following the NEMA protocol, the image spatial resolution obtained from FBP 3DRP reconstruction is shown in figures 5 and 6. For the LYSO-LYSO coincidences, the spatial resolution has a range of 1.27 mm to 2.72 mm,

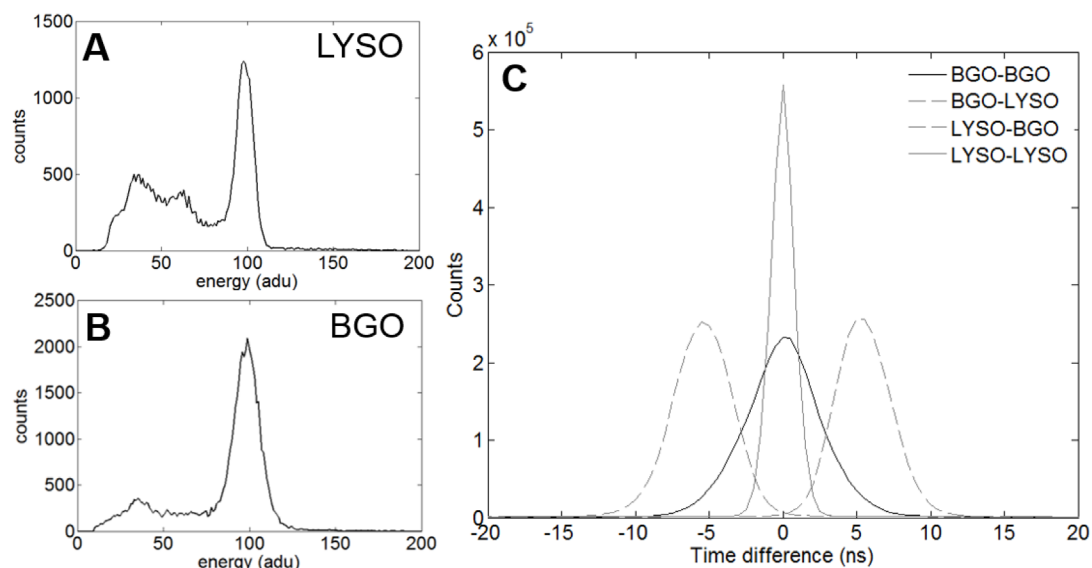


**Figure 3.** Energy spectra of LYSO (A) and BGO (B) events representing the average energy resolution, and timing spectra for different event types (C).

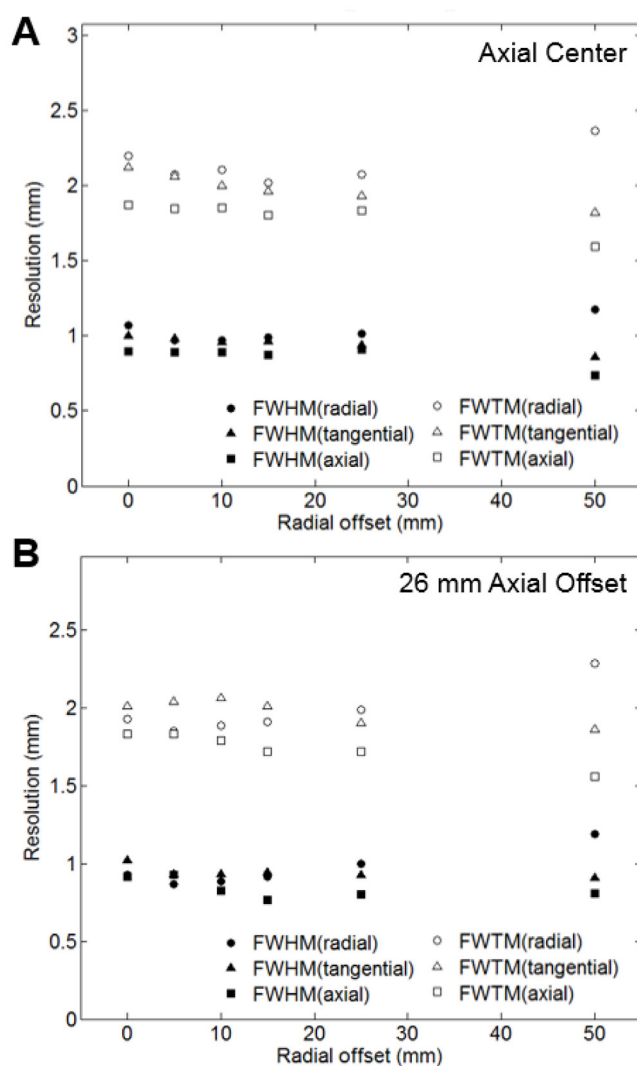
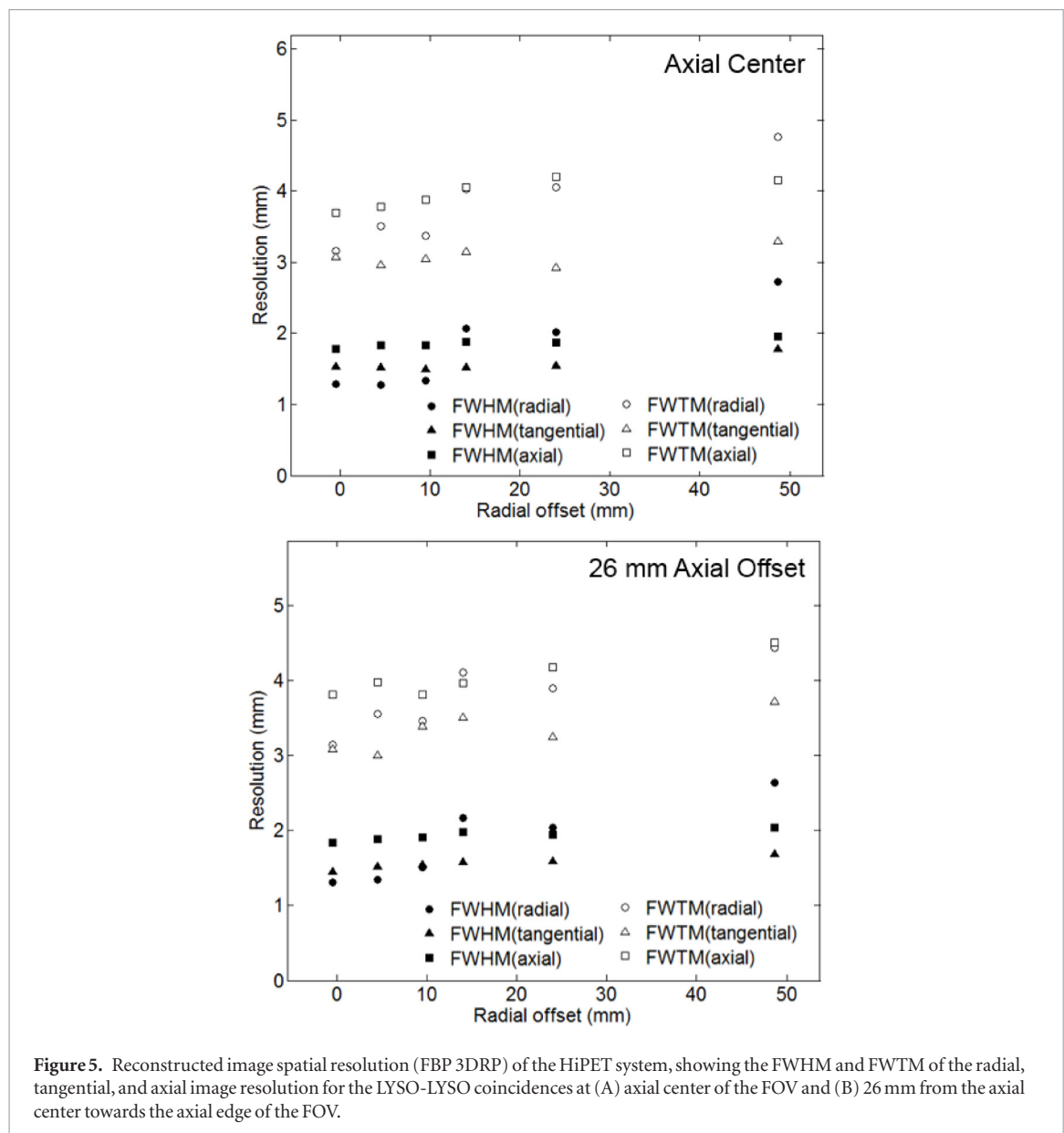


**Figure 4.** Reconstructed image spatial resolution (3D OSEM) of the HiPET system, showing the FWHM and FWTM of the radial, tangential, and axial image resolution at (A) axial center of the FOV and (B) 26 mm from the axial center towards the edge of the FOV.



with an average value of  $1.76 \pm 0.34$  mm. The FWTM has a range of 3.14 mm to 4.77 mm, with an average value of  $3.66 \pm 0.49$  mm. For the BGO-BGO coincidences, the spatial resolution has a range of 1.91 mm to 2.98 mm, with an average value of  $2.32 \pm 0.26$  mm. The FWTM has a range of 4.14 mm to 4.97 mm, with an average value of  $4.56 \pm 0.20$  mm.

### Sensitivity

Table 2 summarizes the absolute system sensitivity for different energy window settings at the CFOV and for the mouse and rat representative lengths. The maximum system sensitivity is 18.6% (including the CLCS events) and 16.5% (excluding the CLCS events) measured at the CFOV and with an LLD of 150 keV. The average sensitivity for a mouse-sized object (7 cm axial length)  $SM_{A,tot}$  ranges from 7.5% to 14.1% (including the CLCS events) and 6.4% to 12.6% (excluding the CLCS events). The average sensitivity for a rat-sized object (10.4 cm system axial length)  $SR_{A,tot}$  ranges from 6.1% to 11.8% (including the CLCS events) and 5.2% to 10.5% (excluding the CLCS events). The axial sensitivity profiles for different energy window settings are shown in figure 7 A (including the CLCS events) and B (excluding the CLCS events).

### Scatter and count-rate performance

The prompt, random and NEC rates as a function of line source activity in the mouse- and rat-sized phantoms are plotted in figures 8(A) and (B). For the mouse-sized phantom, the peak NECR is 179 kcps at a total phantom activity of 12.4 MBq and the SF is 6.9%. For the rat-sized phantom, the peak NECR is 63 kcps at a total phantom activity of 11.3 MBq and the SF is 18.3%.

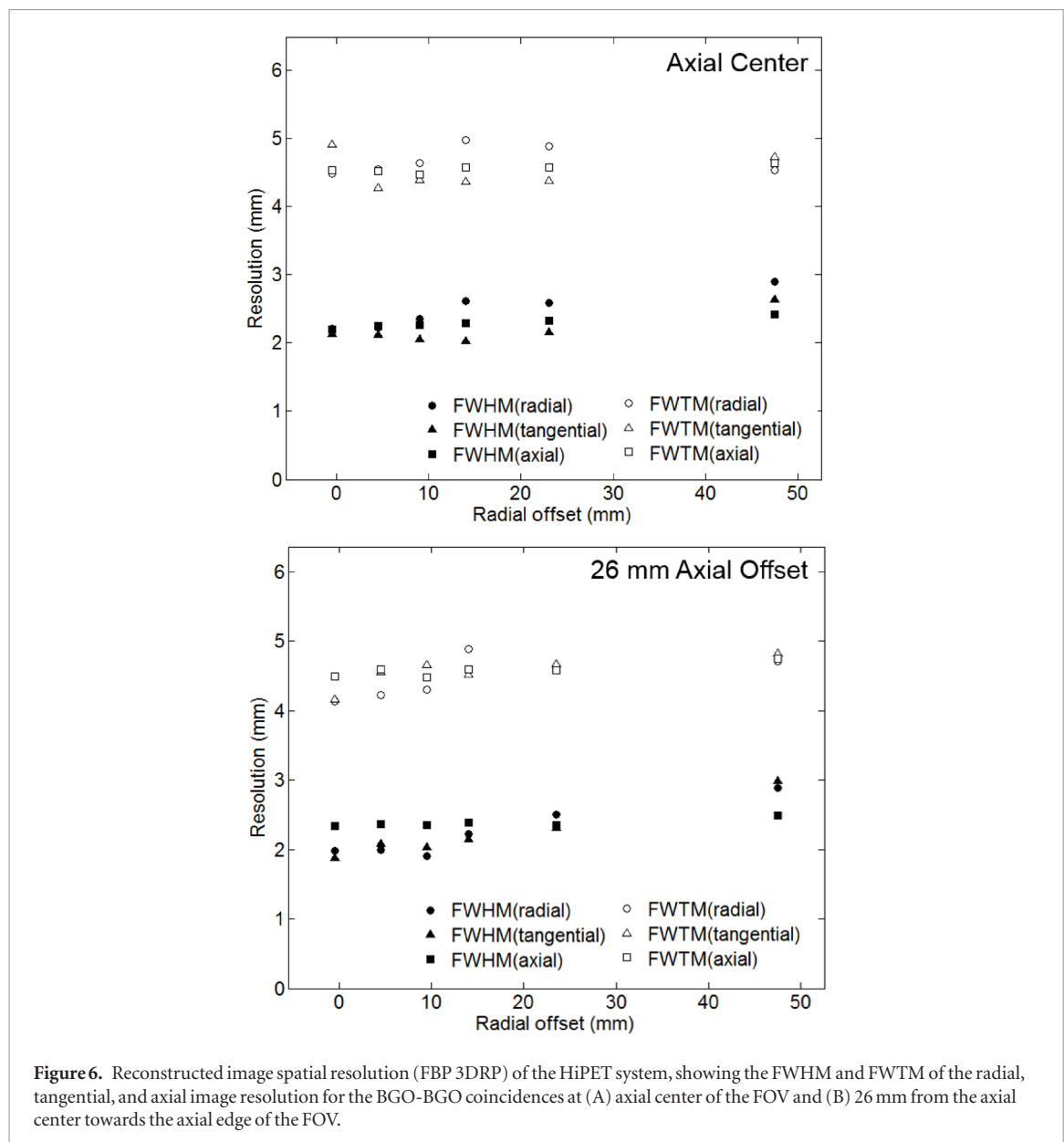


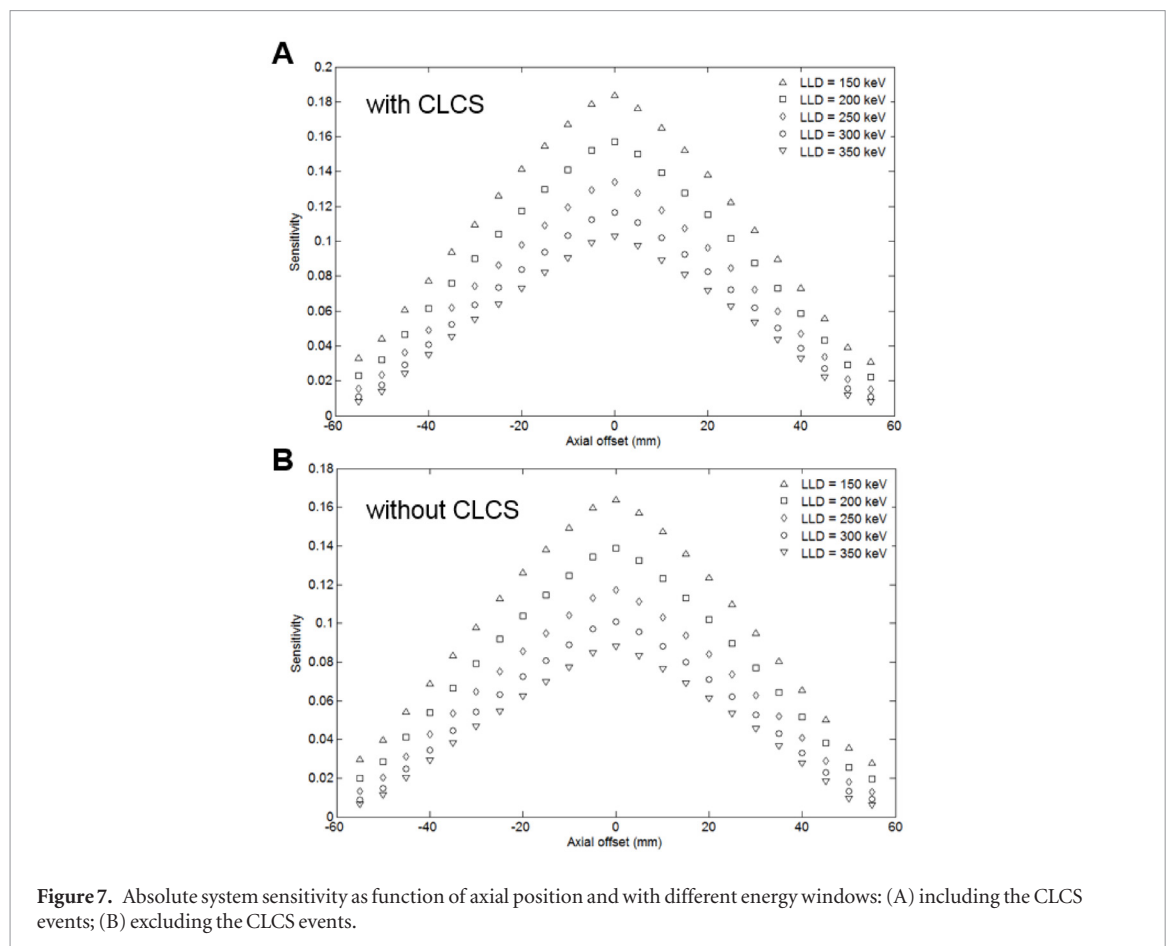
**Table 2.** Absolute system sensitivity (%) as a function of LLD at the axial center of the FOV, for the mouse and rat representative lengths, and including or excluding the CLCS events.

LLD (keV)		150	200	250	300	350
No CLCS	$S_{A,CFOV}$ (%)	16.5	13.9	11.8	10.2	8.9
	$SM_{A,tot}$ (%)	12.6	10.5	8.7	7.4	6.4
	$SR_{A,tot}$ (%)	10.5	8.6	7.1	6.0	5.2
	$S_{A,CFOV}$ (%)	18.6	15.9	13.5	11.8	10.4
With CLCS	$SM_{A,tot}$ (%)	14.1	11.8	10.0	8.6	7.5
	$SR_{A,tot}$ (%)	11.8	9.8	8.1	7.0	6.1

## Imaging studies

### NEMA image quality phantom study

Figure 9 shows images (single slice, 0.27 mm thick) of a transverse plane of the uniform region (A), a transverse plane with the five resolution recovery rods (B), a coronal plane (C), and a profile across the uniform area (D) of the NEMA image quality phantom. With the 3D OSEM reconstruction, the SD in the uniform region was 5.8%. The RCs for the five different rod sizes from 1 to 5 mm diameter were  $0.31 \pm 0.07$ ,  $0.78 \pm 0.08$ ,  $0.84 \pm 0.07$ ,  $0.93 \pm 0.09$  and  $0.92 \pm 0.07$ . The SORs measured in the water and air filled cold region chambers were  $4.7\% \pm 0.9\%$  and  $4.4\% \pm 1.1\%$ .



#### Hot rod phantom

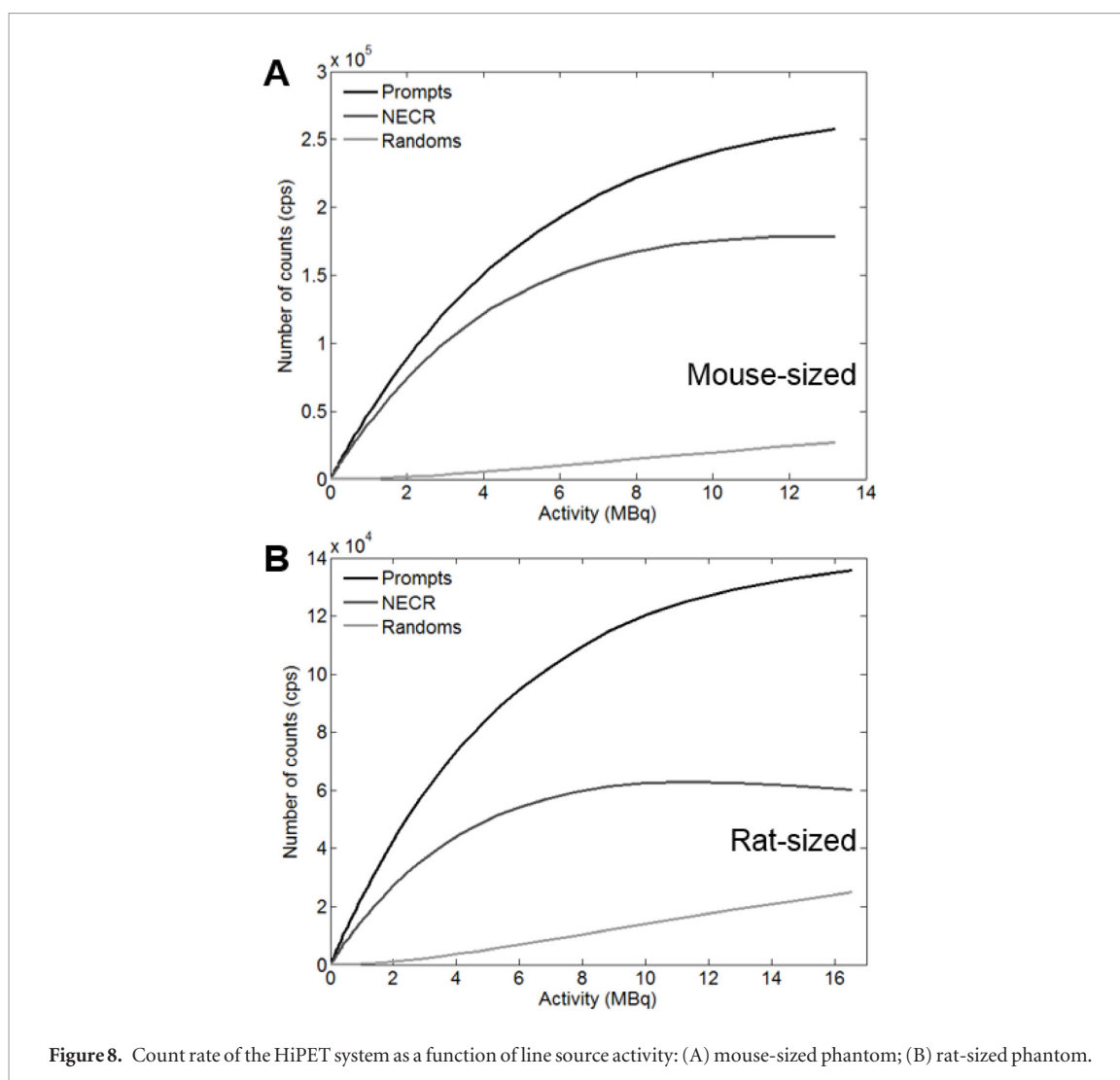
Figure 10 shows a transverse slice of the reconstructed image of the Derenzo style hot rod phantom (0.93 MBq  $^{18}\text{F}$ , 109 min) with 24 iterations of 3D OSEM. The total number of true counts was 140 M. Although the positron range and photon non-collinearity are not corrected, all the rods with 1.0 mm diameter are resolvable in the reconstructed image.

#### Mouse study

Representative images of the biodistribution of [ $^{18}\text{F}$ ]FDG in a mouse are shown in figure 11. Images show coronal and sagittal images from a 20 min [ $^{18}\text{F}$ ]FDG study in a C57BL6 mouse, distinguishing the myocardium from blood pool and identifying other tissues such as Harderian glands, cerebellum, intestines, kidney cortex, kidney medulla and bladder. The activity in the entire subject was approximately 7.33 MBq (198  $\mu\text{Ci}$ ) at scan time.

## Discussion

In this work, we evaluated the performance of the HiPET preclinical PET system using the NEMA NU 4-2008 standards and performed additional phantom and rodent studies. The HiPET system is a new high sensitivity and high spatial resolution preclinical PET tomograph with DOI capability implemented through a dual layer LYSO/BGO phoswich scintillator detector. LYSO and BGO are the most common scintillator materials for PET detectors. Their high effective atomic Z (62 and 75) and high density ( $7.3\text{ g cm}^{-3}$  and  $7.13\text{ g cm}^{-3}$ ) yield high sensitivity, with reduced DOI effect due to moderate crystal penetration. LYSO has a considerably faster decay time ( $\sim 40\text{ ns}$  time constant for lutetium-based versus  $300\text{ ns}$  time constant for BGO), and higher scintillation light yield, leading to better coincidence timing resolution. In comparison, BGO provides a superior attenuation coefficient for annihilation gamma photons and a higher photoelectric fraction with no intrinsic background radiation, in addition to its considerably lower price. To our knowledge, HiPET is the first PET scanner that employs both LYSO and BGO as the detector materials. The average LYSO energy resolution of the 511 keV photopeak was 11.7% for HiPET, which outperforms that of the Inveon (14.6%) (Bao *et al* 2009) or the NanoPET (19%) systems (Szanda *et al* 2011). The BGO energy resolution of the 511 keV photopeak was 17.0% for HiPET, better than that of the PETBox4 (18%) (Gu *et al* 2013) or the G8 (19.3%) (Gu *et al* 2019) which are two BGO PET systems developed by our group. The improvement on energy resolution is mainly due to the higher first



photoelectron collection efficiency of the H12700 MAPMT, and the use of the tapered, multi-element light guides which improves the uniformity of light collection.

The HiPET scanner utilizes a LYSO/BGO phoswich dual layer detector configuration to permit DOI correction by measuring differences in light decay time between different scintillators. Improved spatial resolution uniformity and reduced parallax error has been achieved in scanners that implemented such phoswich detector approaches compared to scanners of single layer design with equivalent scintillator volume and no DOI capability (Seidel *et al* 2003, Wang *et al* 2006, de Jong *et al* 2007, Roldan *et al* 2007). With iterative reconstructions that model the DOI-capable detectors in the system response matrix, the resolution of HiPET is approximately isotropic and spatially invariant throughout the entire FOV and has minimal degradation from DOI, providing a large FOV for imaging of larger rodents. A submillimeter volumetric spatial resolution has been achieved for HiPET primarily attributable to the fine pitch (1.08 mm) of the LYSO crystals. The superior spatial resolution of HiPET yields RC of 0.78 and 0.31 for the 2 mm and 1 mm rods of the image quality phantom, while rod sizes as small as 1 mm can be resolved in the hot rod phantom image. This is particularly advantageous for imaging mice and small tissues of interest, where high spatial resolution should alleviate partial volume effects allowing for detection of smaller or lower-contrast structures with improved quantification in both static and dynamic scans.

Following the NEMA NU-4 standard which indicates FBP as the reconstruction algorithm for the spatial resolution measurements, the FBP 3DRP result is reported in figures 5 and 6. No correction was performed for the size and shape of the source, positron range, and non-collinearity of positron annihilation. The system geometry of the HiPET is a decagon consisting of twenty flat panel detectors arranged in two rings, which is only a rough approximation of a ring geometry. Such a decagon configuration results in significant parallax error near the CFOV compared to scanners with a more uniform ring-like geometry. As a result, the spatial resolution measured from the FBP 3DRP reconstructed images suffers from star-like artifacts and non uniform sampling caused by the radial in-plane gaps between detector modules. The compromise of spatial resolution and image artifacts in the FBP reconstructed images were also observed in Hallen *et al* (2018) where a similar decagon system geometry was employed. The resolution degradation was only evident in the FBP 3DRP reconstruction, while the

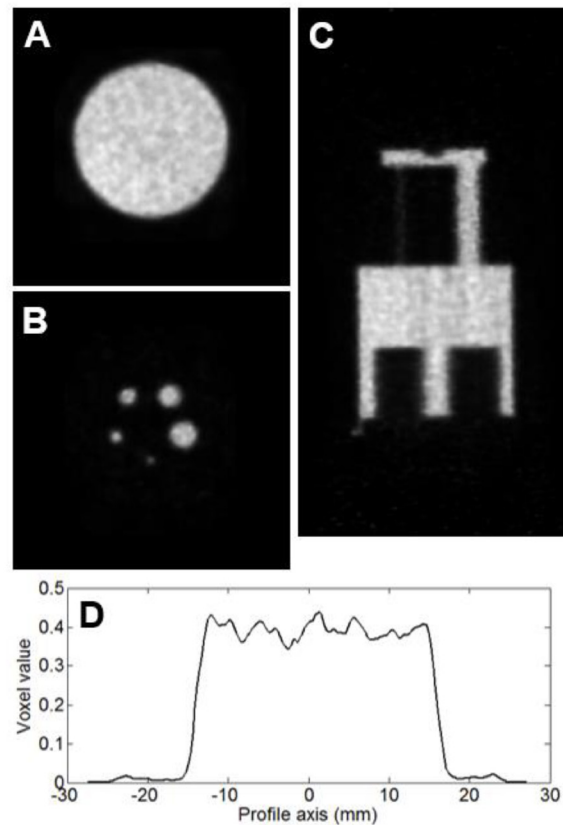


**Figure 9.** Reconstructed Images of the NEMA NU-4 image quality phantom, filled with  $^{18}\text{F}$  (3.7 MBq) and imaged for 20 min: (A) a transverse slice of the uniform region; (B) a transverse slice of the rods region; (C) a coronal slice; (D) a profile across the uniform area.

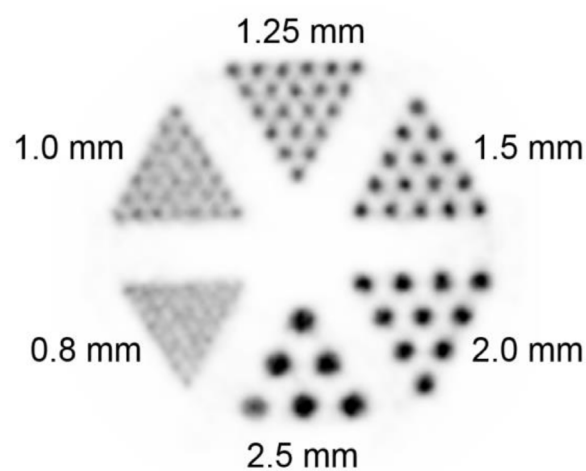
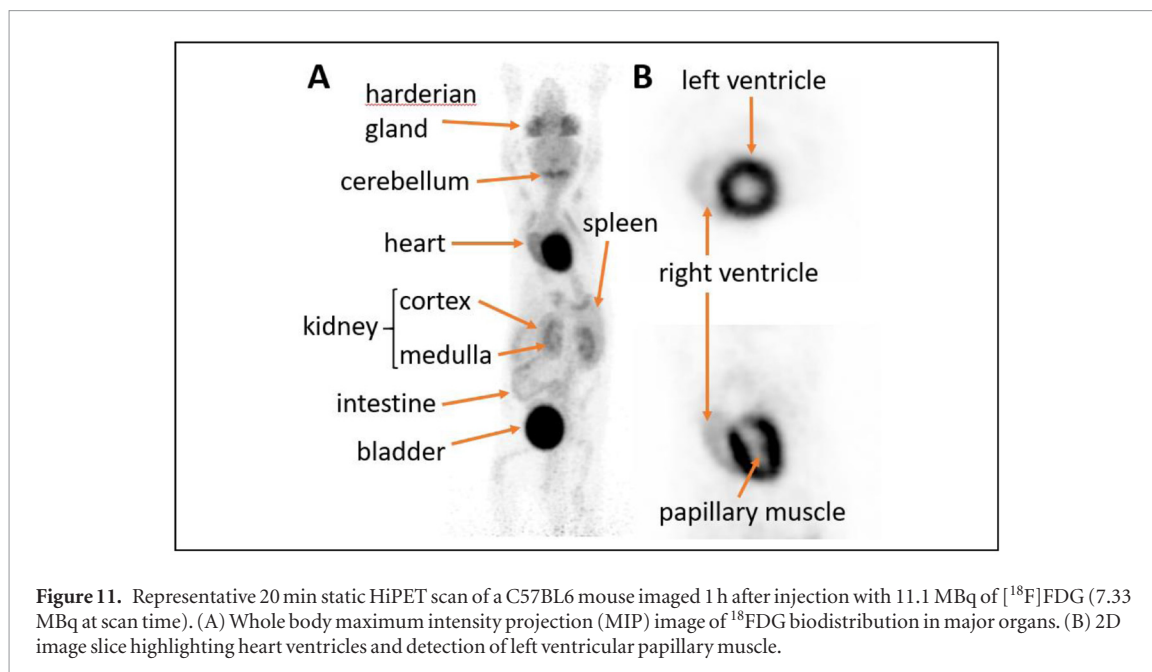


**Figure 10.** A transverse slice of the reconstructed image of the Derenzo style hot rod phantom (0.8, 1.0, 1.25, 1.5, 2.0, 2.5 mm) imaged for 109 min and reconstructed with 3D OSEM (10 subsets) with 24 OSEM iterations.

iterative 3D OSEM image reconstruction accurately models the physical response of the scanner in the system matrix and compensates for the nonuniform sampling and missing data, leading to significant improvement on spatial resolution in all three directions and throughout the FOV, as shown in figure 4. To represent a more realistic measure of spatial resolution similar to what is used for animal imaging, the hot rod phantom reconstructed with the OSEM reconstruction shows a submillimeter image spatial resolution with a good separation of rods with diameters of 1.0 mm.

One of the innovative design features of the HiPET system is its capability of identifying CLCS events. Existing studies have shown that the capability of rejecting ICS events, or estimating the first interaction site of an ICS event yields improved image quality and quantification (Comanor *et al* 1996, Shao *et al* 1996, Miyaoka and Lewellen 2000, Pratz and Levin 2009, Gu *et al* 2010, Ritzer *et al* 2017). This is in agreement with our preliminary studies (not



shown in this work). In this work, the CLCS events were excluded for all the phantom and *in vivo* scans reported. Nevertheless, the resolution improvement by excluding the CLCS events was achieved at the price of compromised sensitivity. Given the large difference of light output between LYSO and BGO, especially within the short pulse integration duration of the low gain path, the position of CLCS events that deposit even a small amount of energy in the LYSO layer is predominantly determined by the LYSO signal. Therefore, most of the CLCS events are positioned closer to the crystal of first interaction (Gu *et al* 2015a). Acceptance of CLCS events as events belonging to the LYSO layer leads to small loss of local contrast, but to an improvement in system sensitivity. The performance capabilities of the HiPET can be improved further if the modeling of the detector response to the CLCS events can be incorporated accurately in the system matrix, details of which are beyond the scope of this work. The HiPET system identified CLCS events using cost effective Anger logic single end readout operated with three channels per detector. The DCI method for event type discrimination is simple and robust, and can be easily implemented in most digital or analog electronic signal processing chains. In comparison, other existing approaches rejecting ICS events, by estimating the first interaction site of an ICS event using selection criteria (Comanor *et al* 1996, Shao *et al* 1996, Miyaoka and Lewellen 2000, Ritzer *et al* 2017) or maximum likelihood based on Compton kinematics (Pratx and Levin 2009, Gu *et al* 2010) require complex data acquisition systems for measuring individual interactions of the ICS events (Vandenbroucke *et al* 2010) and entail significant computational efforts for determining the location of first interaction (Pratx and Levin 2009, Gross-Weege *et al* 2016).

High photon detection sensitivity is required to reconstruct quantitative images at high spatial resolution (Habte *et al* 2007). The DOI and CLCS identification capability of the HiPET allows the use of a total detector thickness of 15 mm for high photon detection sensitivity while maintaining high detection accuracy. The tapered, multiple element glass lightguide (Gu *et al* 2015b) used in the HiPET detector enables the use of scintillator arrays with overall dimensions of  $52 \times 52 \text{ mm}^2$  that match the external dimensions of the MAPMT package, allowing the arrangement of multiple detector rings without axial gaps between them. The 104 mm axial FOV of HiPET is 11% larger than that of the NanoPET (94 mm) (Szanda *et al* 2011, Nagy *et al* 2013) which uses PMTs of the same external dimension, resulting in larger solid detectable angle and higher sensitivity. The absolute sensitivity of the HiPET at CFOV is 13.5% and 10.4% for the 250 and 350 keV LLD (CLCS events included), which outperforms most of the state-of-the-art preclinical scanners (Goertzen *et al* 2012), such as the Inveon PET (6.72% at 350–625 keV) (Bao *et al* 2009) or the NanoScan sequential PET/MRI (8.4% at 250–750 keV) (Nagy *et al* 2013). According to the NEMA NU4 protocols the sensitivity values are not corrected for the attenuation from the source container. If a 12% sensitivity loss as the effect of the attenuation from the acrylic cube surrounding the source is considered (Szanda *et al* 2011), the sensitivity of the HiPET at CFOV can be rescaled to 15.1% and 11.6% for the 250 and 350 keV LLD, respectively.

The measured coincidence timing resolution of the HiPET system was 2.2, 4.8 and 6.6 ns for LYSO-LYSO, LYSO-BGO and BGO-BGO coincidences, respectively. The event time stamp of the HiPET was extracted using the energy sum signal, instead of the fast dynode signal. The energy signal passes through an analog low pass filter in the front end electronics for accurate signal digitization, while the constant fraction discriminator (CFD) used for time stamp pick-off does not allow triggering at a low level for optimal timing, compromising timing resolution. The advantage of this approach is that the total number of readout channels is reduced by 25%, from

80 to 60 by using three channels per detector, reducing the system complexity and electronics cost. The timing resolution for BGO is worse than that for LYSO due to its slower decay time and lower light output. It is important to note here that recent work shows unprecedented timing resolution in BGO based on Cherenkov emission (Kwon *et al* 2016, Brunner and Schaart 2017), indicating the potential for improved BGO timing resolution in the future. A good timing resolution allows the reduction of random events by shortening the coincidence time window. However, benefits of time of flight (TOF) information with current technologies will not be substantial in preclinical imaging due to the small ring geometry. Nevertheless, the timing resolution of the HiPET is still acceptable for non-TOF PET timing.

The peak NECR of the HiPET was achieved at a total phantom activity of 12.4 MBq at which point the limit for the electric current flowing through the PMT was reached. At this high current, the detector gain was reduced and the energy of the detected events progressively fell out of the preset energy window. This limitation could potentially be alleviated by moving some of the overall amplification, from the PMT to the front end analog electronics. By using a lower high voltage for the PMT and a readout with higher amplification, or using PMTs with lower gain, significant improvements in the overall system dynamic range may be possible. The second count rate bottleneck after the PMT current limit is the signal pulse integration time and the ensuing deadtime of the detector readout, which is currently less than 1  $\mu$ s combined (240 ns for LYSO and 1000 ns for BGO). The activity of 12.4 MBq at the peak NECR corresponds to a singles rate of approximately 340 kcps per detector, which is well below the deadtime of the detector. This indicates the potential for significant improvements and optimizations. Nevertheless, the current activity at peak NECR of the HiPET is more than sufficient for most mouse applications where typical injected activities are in the 1–10 MBq range. The peak NECR of the HiPET (179 kcps at 12.4 MBq) is lower than that of the Inveon system (1670 kcps at 131 MBq) (Bao *et al* 2009), while for a 12 MBq injection, the NECR values for the HiPET and Inveon were comparable. Imaging applications with rats and larger animals could benefit from a count rate peak at higher activities.

The imaging protocols including energy window and timing window and the CLCS event acceptance policy for the HiPET are currently being optimized to improve imaging quality. A 350 keV LLD was used for all the phantom and *in vivo* scans in this work. Details of the optimization are beyond the scope of this work and will be presented in a future study.

## Conclusion

This study evaluated the performance of the HiPET prototype preclinical PET tomograph using the NEMA NU 4 standards. For an energy window of 250 and 350–650 keV, the peak absolute sensitivity at the center of the FOV was 13.5% and 10.4% including CLCS events, and 11.8% and 8.9% excluding CLCS events, respectively. The FWHM in the OSEM reconstructed image of a point source in air, ranges from 0.73 mm to 1.19 mm, with an average value of  $0.93 \pm 0.09$  mm, and the volumetric resolution ranges from 0.66 to 0.96  $\mu$ l. The peak NECR and SF were 179 kcps at 12.4 MBq and 6.9% for the mouse-sized phantom, and 63 kcps at 11.3 MBq and 18.3% for the rat-sized phantom. The HiPET scanner utilizes phoswich LYSO/BGO dual layer detectors to permit DOI and CLCS measurement and achieves near submillimeter and uniform spatial resolution over the imaging FOV and a superior sensitivity. The overall performance demonstrates that the HiPET system produces high quality images for molecular imaging in biomedical research.

## Acknowledgments

The authors would like to thank the staff of the UCLA Ahmanson Biomedical Cyclotron Facility for providing  $^{18}\text{F}$ -ion and  $^{18}\text{F}$ -FDG. We would like to thank Dishan Abeydeera of the Crump Institute's Preclinical Imaging Technology Center for his assistance with the *in vivo* images for this study. This work was supported by the UCLA Foundation from a donation made by Ralph and Marjorie Crump for the UCLA Crump Institute for Molecular Imaging and in part by the National Cancer Institute P30 CA016042 Cancer Center Support Grant.

## Disclosure

Nam T Vu and Zheng Gu are currently employees of Sofie Biosciences, Inc. Nam T Vu and Arion F Chatzioannou are shareholders of Sofie Biosciences, Inc.

The detector technology described in this work is patented by the Regents of University of California (Hadjioannou *et al* 2019)

No other potential conflicts of interest relevant to this article exist.

## References

- Anger H O 1958 Scintillation camera *Rev. Sci. Instrum.* **29** 27–33
- Bao Q, Newport D, Chen M, Stout D B and Chatzioannou A F 2009 Performance evaluation of the in vivo dedicated PET preclinical tomograph based on the NEMA NU-4 standards *J. Nucl. Med.* **50** 401–8
- Brunner S E and Schaart D R 2017 BGO as a hybrid scintillator/Cherenkov radiator for cost-effective time-of-flight PET *Phys. Med. Biol.* **62** 4421–39
- Chatzioannou A F 2002 Molecular imaging of small animals with dedicated PET tomographs *Eur. J. Nucl. Med.* **29** 98–114
- Cherry S R 2004 *In vivo* molecular and genomic imaging: new challenges for imaging physics *Phys. Med. Biol.* **49** R13–48
- Cherry S R 2006 The 2006 Henry N Wagner lecture: of mice and men (and positrons)—advances in PET imaging technology *J. Nucl. Med.* **47** 1735–45
- Comanor K A, Virador P R G and Moses W W 1996 Algorithms to identify detector Compton scatter in PET modules *IEEE Trans. Nucl. Sci.* **43** 2213–8
- Cox B L et al 2016 Development of a novel linearly-filled Derenzo microPET phantom *Am. J. Nucl. Med. Mol. Imaging* **6** 199–204
- de Jong H W A M, van Velden F H P, Kloet R W, Buijs F L, Boellaard R and Lammertsma A A 2007 Performance evaluation of the ECAT HRRT: an LSO-LYSO double layer high resolution, high sensitivity scanner *Phys. Med. Biol.* **52** 1505–26
- Du H N, Yang Y F, Glodo J, Wu Y B, Shah K and Cherry S R 2009 Continuous depth-of-interaction encoding using phosphor-coated scintillators *Phys. Med. Biol.* **54** 1757–71
- Goertzen A L et al 2012 NEMA NU 4-2008 Comparison of preclinical PET imaging systems *J. Nucl. Med.* **53** 1300–9
- Gross-Weege N, Schug D, Hallen P and Schulz V 2016 Maximum likelihood positioning algorithm for high-resolution PET scanners *Med. Phys.* **43** 3049–61
- Gu Y, Prax G, Lau F W Y and Levin C S 2010 Effects of multiple-interaction photon events in a high-resolution PET system that uses 3D positioning detectors *Med. Phys.* **37** 5494–508
- Gu Y et al 2011 Study of a high-resolution, 3D positioning cadmium zinc telluride detector for PET *Phys. Med. Biol.* **56** 1563–84
- Gu Z, Prout D L, Silverman R W, Herman H, Dooraghi A and Chatzioannou A F 2015a A DOI detector with crystal scatter identification capability for high sensitivity and high spatial resolution PET imaging *IEEE Trans. Nucl. Sci.* **62** 740–7
- Gu Z, Prout D L, Valenciga Y and Chatzioannou A F 2015b Lightguides for improving edge crystal identification and energy resolution in pixelated scintillator detectors *IEEE Nuclear Science Symp. Conf. Record* (<https://doi.org/10.1109/nssmic.2015.7582086>)
- Gu Z et al 2013 NEMA NU-4 performance evaluation of PETbox4, a high sensitivity dedicated PET preclinical tomograph *Phys. Med. Biol.* **58** 3791–814
- Gu Z et al 2019 Performance evaluation of G8, a high-sensitivity benchtop preclinical PET/CT tomograph *J. Nucl. Med.* **60** 142–9
- Habte F, Foudray A M K, Olcott P D and Levin C S 2007 Effects of system geometry and other physical factors on photon sensitivity of high-resolution positron emission tomography *Phys. Med. Biol.* **52** 3753–72
- Hadjioannou A-X, Gu Z and Prout D 2019 Multiple spatial resolution scintillation detectors *Google Patents*, US 10,234,572
- Hallen P et al 2018 PET performance evaluation of the small-animal Hyperion IID PET/MRI insert based on the NEMA NU-4 standard *Biomed. Phys. Eng. Express* **4**
- Hoffman E J, Guerrero T M, Germano G, Digby W M and Dahlbom M 1989 PET system calibrations and corrections for quantitative and spatially accurate images *IEEE Trans. Nucl. Sci.* **36** 1108–12
- Inadama N et al 2006 8-layer DOI encoding of 3-dimensional crystal array *IEEE Trans. Nucl. Sci.* **53** 2523–8
- Kinahan P E and Rogers J G 1989 Analytic 3d image-reconstruction using all detected events *IEEE Trans. Nucl. Sci.* **36** 964–8
- Kwon S I, Gola A, Ferri A, Piemonte C and Cherry S R 2016 Bismuth germanate coupled to near ultraviolet silicon photomultipliers for time-of-flight PET *Phys. Med. Biol.* **61** L38–47
- Levin C S, Tornai M P, Cherry S R, MacDonald L R and Hoffman E J 1997 Compton scatter and x-ray crosstalk and the use of very thin intercrystal septa in high-resolution PET detectors *IEEE Trans. Nucl. Sci.* **44** 218–24
- Lewellen T K 2008 Recent developments in PET detector technology *Phys. Med. Biol.* **53** R287–317
- Ling T, Lewellen T K and Miyaoka R S 2007 Depth of interaction decoding of a continuous crystal detector module *Phys. Med. Biol.* **52** 2213–28
- Loening A M and Gambhir S S 2003 AMIDE: a free software tool for multimodality medical image analysis *Mol. Imaging* **2** 131–7
- McElroy D P, Pimpl W, Pichler B J, Rafecas M, Schuler T and Ziegler S I 2005 Characterization and readout of MADPET-II detector modules: validation of a unique design concept for high resolution small animal PET *IEEE Trans. Nucl. Sci.* **52** 199–204
- Miyaoka R S and Lewellen T K 2000 Effect of detector scatter on the decoding accuracy of a DOT detector module *IEEE Trans. Nucl. Sci.* **47** 1614–9
- Moses W W and Derenzo S E 1994 Design studies for a pet detector module using a pin photodiode to measure depth of interaction *IEEE Trans. Nucl. Sci.* **41** 1441–5
- Mosset J B et al 2006 Development of an optimized LSO/LuYAP phoswich detector head for the Lausanne ClearPET demonstrator *IEEE Trans. Nucl. Sci.* **53** 25–9
- Mumcuoglu E U, Leahy R, Cherry S R and Zhou Z Y 1994 Fast gradient-based methods for Bayesian reconstruction of transmission and emission pet images *IEEE Trans. Med. Imaging* **13** 687–701
- Murayama H, Ishibashi H, Uchida H, Omura T and Yamashita T 1998 Depth encoding multicrystal detectors for PET *IEEE Trans. Nucl. Sci.* **45** 1152–7
- Nagy K et al 2013 Performance evaluation of the small-animal nanoScan PET/MRI system *J. Nucl. Med.* **54** 1825–32
- National Electrical Manufacturers Association 2008 *Performance Measurements of Small Animal Positron Emission Tomographs (NEMA Standards Publication NU 4-2008)* (Rosslyn, VA: NEMA)
- Phelps M E 2000 Positron emission tomography provides molecular imaging of biological processes *Proc. Natl Acad. Sci. USA* **97** 9226–33
- Prax G and Levin C S 2009 Bayesian reconstruction of photon interaction sequences for high-resolution PET detectors *Phys. Med. Biol.* **54** 5073–94
- Ritzer C, Hallen P, Schug D and Schulz V 2017 Intercrystal scatter rejection for pixelated PET detectors *IEEE Trans. Radiat. Plasma Med. Sci.* **1** 191–200
- Roldan P S et al 2007 Raytest ClearPET (TM), a new generation small animal PET scanner *Nucl. Instrum. Methods Phys. Res. A* **571** 498–501
- Saoudi A et al 1999 Investigation of depth-of-interaction by pulse shape discrimination in multicrystal detectors read out by avalanche photodiodes *IEEE Trans. Nucl. Sci.* **46** 462–7
- Seidel J, Vaquero J J and Green M V 2003 Resolution uniformity and sensitivity of the NIH ATLAS small animal PET scanner: comparison to simulated LSO scanners without depth-of-interaction capability *IEEE Trans. Nucl. Sci.* **50** 1347–50

- Seidel J, Vaquero J J, Siegel S, Gandler W R and Green M V 1999 Depth identification accuracy of a three layer phoswich PET detector module *IEEE Trans. Nucl. Sci.* **46** 485–90
- Shao Y P, Cherry S R, Siegel S and Silverman R W 1996 Study of inter-crystal scatter in small scintillator arrays designed for high resolution PET imaging *IEEE Trans. Nucl. Sci.* **43** 1938–44
- Shao Y P, Sun X S, Lan K J A, Bircher C, Lou K and Deng Z 2014 Development of a prototype PET scanner with depth-of-interaction measurement using solid-state photomultiplier arrays and parallel readout electronics *Phys. Med. Biol.* **59** 1223–38
- Siegel S, Silverman R W, Shao Y P and Cherry S R 1996 Simple charge division readouts for imaging scintillator arrays using a multi-channel PMT *IEEE Trans. Nucl. Sci.* **43** 1634–41
- Szanda I et al 2011 National Electrical Manufacturers Association NU-4 performance evaluation of the PET component of the nanoPET/CT preclinical PET/CT scanner *J. Nucl. Med.* **52** 1741–7
- Taschereau R, Vu N T and Chatzioannou A F 2014 Calibration and data standardization of a prototype bench-top preclinical CT 2014 *IEEE Nucl. Science Symp. and Medical Imaging Conf. (NSS/MIC)* (<https://doi.org/10.1109/nssmic.2014.7430845>)
- Tsuda T et al 2004 A four-layer depth of interaction detector block for small animal PET *IEEE Trans. Nucl. Sci.* **51** 2537–42
- Vandenbroucke A, Foudray A M K, Olcott P D and Levin C S 2010 Performance characterization of a new high resolution PET scintillation detector *Phys. Med. Biol.* **55** 5895–911
- Wang Y C, Seidel J, Tsui B M W, Vaquero J J and Pomper M G 2006 Performance evaluation of the GE healthcare eXplore VISTA dual-ring small-animal PET scanner *J. Nucl. Med.* **47** 1891–900
- Weissleder R and Mahmood U 2001 Molecular imaging *Radiology* **219** 316–33
- Wong W H 1986 Designing a stratified detection system for PET cameras *IEEE Trans. Nucl. Sci.* **33** 591–6
- Yamamoto S and Ishibashi H 1998 A GSO depth of interaction detector for PET *IEEE Trans. Nucl. Sci.* **45** 1078–82
- Yang Y F et al 2006 Depth of interaction resolution measurements for a high resolution PET detector using position sensitive avalanche photodiodes *Phys. Med. Biol.* **51** 2131–42
- Yazaki Y et al 2012 Development of the X'tal cube: a 3D position-sensitive radiation detector with all-surface MPPC readout *IEEE Trans. Nucl. Sci.* **59** 462–8
- Zhang N, Thompson C J, Cayouette F, Jolly D and Kecani S 2003 A prototype modular detector design for high resolution positron emission mammography imaging *IEEE Trans. Nucl. Sci.* **50** 1624–9